Chinese Chemical Letters 32 (2021) 1055–1060

Contents lists available at ScienceDirect

Chinese Chemical Letters

journal homepage: www.elsevier.com/locate/cclet

Communication

Polydopamine (PDA)-activated cobalt sulfide nanospheres responsive to tumor microenvironment (TME) for chemotherapeutic-enhanced photothermal therapy

Mengmeng Hou[a,1], Yuanxin Zhong[a,1], Lei Zhang[b], Zhigang Xu[a], Yuejun Kang[a], Peng Xue[a,*]

[a] School of Materials and Energy, Southwest University, Chongqing 400715, China
[b] State Key Laboratory of Silkworm Genome Biology, Southwest University, Chongqing 400716, China

ARTICLE INFO

Article history:
Received 24 June 2020
Received in revised form 21 July 2020
Accepted 6 August 2020
Available online 8 August 2020

Keywords:
Cobalt sulfide nanospheres
Polydopamine
Tumor microenvironment
Drug delivery
Combination therapy

ABSTRACT

Most recently, cobalt sulfide (CoS) nanospheres (NSs) have been demonstrated as an ideal high-efficient photothermal agent for tumor elimination. However, the surface of CoS NSs is lack of functional chemical groups or active radicals to incorporate therapeutic agents, which tremendously hinders their versatile utilization in medical field. Here, surface activation of CoS NSs was realized through the growth of polydopamine (PDA) *in situ via* alkaline-triggered polymerization. Upon the formation of CoS@PDA NSs, thiol-polyethylene glycol (SH-PEG) and chemotherapeutic agent of doxorubicin (DOX) were loaded onto the particle surface by means of π-π electrostatic interaction and Michael addition reactions. As-synthesized CoS@PDA/PEG/DOX (CoPPD) NSs exhibited an admirable photothermal property and high loading capacity of DOX (44.6%). Furthermore, drug release can be accelerated under a more acidic pH condition mimicking tumor microenvironment (TME), ascribed to the protonation of amino group in DOX molecules. Finally, a strong chemotherapeutic-enhanced photothermal therapeutic effect was demonstrated toward solid tumor under near-infrared (NIR) light irradiation without causing significant systemic toxicity. In this regard, this paradigm may offer valuable guidance for the design of multifunctional CoS-based nanoagents for medical treatment.

Cancer has been recognized as a grim fatal disease globally, and the incidence continuously rises in recent years, whose high mortality seriously threatens human health [1,2]. To effectively tackle cancer, minimal-invasive treatment modalities have aroused rapid increasing attention in this study field, because of their versatility in tumor-target administration, spatiotemporal adjustability and alleviative adverse effects towards healthy tissues [3–5]. Amongst them, thermal ablation and derivative photo-induced thermotherapy (PTT) have sparked growing interests as non-invasive oncotherapy to satisfy the unmet clinical demand, with the aid of photoactive agents [6–8]. To be a eligible photothermal agent (PTA), one should have satisfactory biocompatibility, long-period stability in physiological condition and undisputed high photothermal conversion efficiency [9,10]. In this regard, a good number of PTAs are popping up to offer more choices for clinical translation [11]. Moreover, mass production with less cost is strongly suggested for industrial manufacture [12]. However, on account of limited tissue penetration caused by light scattering, it has become dramatically difficult to completely ablate solid tumor with single PTT, particularly with regard to deep-rooted tissues [13,14]. Fortunately, chemotherapeutic-enhanced photothermal therapy (PTT) mediated by relevant drugs always produces remarkable treatment effects, thanks to a powerful synergistic effect [15–20]. Thus far, plenty PTAs, involving inorganic nanomaterials (gold- [21,22], carbon- [23], transition-metal chalcogenide- [24–26] and MoS_2 nanostructures [27]) and organic nanocomplex (polypyrrole [28,29], polyaniline [30] and porphysomes [31]), have been developed for thermal-induced tumor destruction upon photo-activation. Nevertheless, versatile nanomaterials concurrently acting as both PTAs and drug carriers are still in demand for dual-modal PTT/chemotherapy.

As one of the most widepreading and earth-abundant element, cobalt, is not only crucial for the synthesis of vitamin B12, essential enzymes and methionine, but also vital for fat metabolism and nerve function [32]. Cobalt chalcogenides,with diversified morphology such as nanowires, nanoflakes and nanospheres, have been extensively exploited as catalysts [33–37], supercapacitors

* Corresponding author.
E-mail address: xuepeng@swu.edu.cn (P. Xue).
[1] These authors contributed equally to this work.

https://doi.org/10.1016/j.cclet.2020.08.009

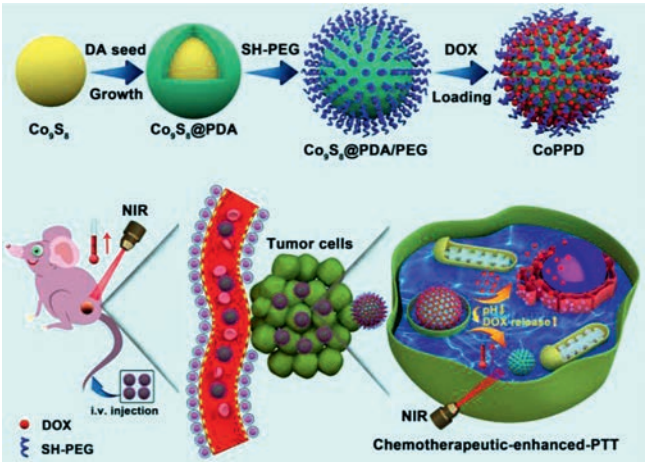

Fig. 1. Schematic diagram of synthsis procedure of CoPPD NSs for chemotherapeutic-enhanced photothermal therapy *in vivo*.

[38,39] and biosensors [40,41], benefitting from their large specific surface area and high electronic conductivity. Moreover, synthetic condition for cobalt chalcogenides is generally mild with good controllability. Most recently, two dimensional Co_9Se_8 nanoplates and spherical CoS_x nanopsheres have been constructed as promising PTAs for tumor theranostics, including precise tumor localization and near-infrared (NIR) activable PTT with great efficiency [42–44]. However, the reported cobalt chalcogenides nanomaterials suffer from undesirable aqueous dispersity and stability. More importantly, the nanostructure surface is deficient in active groups or radicals for the modification of therapeutic agents, which undoubtedly impedes the relevant medical applications [45]. In this regard, facile and simple strategies are highly recommended to be put forward to active the surface of cobalt chalcogenides for postsynthetic functionalization. On the other hand, dopamine (DA), as a well-known neurotransmitte, can form quinone through the oxidation of catechol. Subsequently, these quinones can conjugate with adjacent catechols and/or quinones to generate a thin layer of polydopamine (PDA) on the solid surface under mild alkaline condition (pH 8–8.5) [46,47]. The reactive quinone groups in PDA provide useful anchoring points for loading drug molecules. Furthermore, bioinspired PDA can significantly improve the biocompatibility of nanocarriers for medical translations [48].

Inspired by the well-defined PDA growth chemistry, we creatively conducted surface activation of Co_9S_8 nanospheres (NSs) through *in situ* polymerization of DA under weak alkalinity (Fig. 1). Beforehand, Co_9S_8 NSs were developed *via* a modified solvothermal-based technique. Upon the formation of Co_9S_8@PDA NSs, a subsequent modification was performed by the conjugation of thiol-polyethylene glycol (SH-PEG) and encapsulation of doxorubicin (DOX, a chemotherapeutic drug). As-generated Co_9S_8@PDA/PEG/DOX (CoPPD) NSs exhibited fascinating capacity

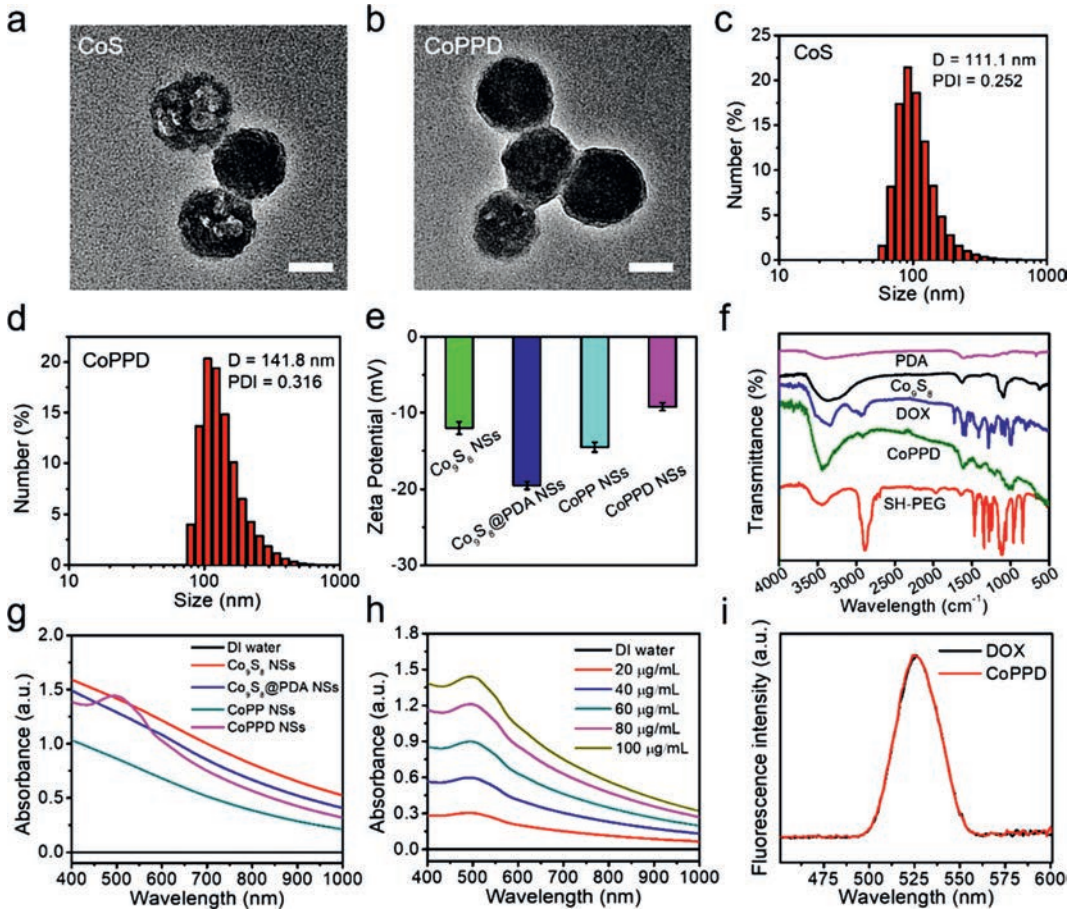

Fig. 2. Physicochemical characterizations. TEM images of (a) Co_9S_8 NSs and (b) CoPPD NSs (scale bar: 50 nm). Size distribution of (c) Co_9S_8 NSs and (d) CoPPD NSs measured by dynamic light scattering (DLS). (e) Surface potential of Co_9S_8, Co_9S_8@PDA, CoPP and CoPPD NSs. (f) FTIR spectra of Co_9S_8 NSs, SH-PEG, DOX and CPPD NSs; (g) UV–vis-NIR spectra of Co_9S_8, Co_9S_8@PDA, CoPP and CoPPD NSs. (h) UV–vis-NIR spectra of CoPPD NSs at different concentrations. (i) Fluorescence emission spectra of free DOX and CoPPD NS aqueous dispersion (equivalent DOX concentration: 20 μg/mL, λ_{ex} = 488 nm).

and stability in hyperthermia generation upon NIR irradiation. In addition, the release of loaded DOX can be promoted under mild acidity mimicking tumor microenvironment (TME). A chemotherapeutic-enhanced PTT effect mediated by CoPPD NSs can be anticipated to effectively suppress the tumor growth and recurrence.

As shown in TEM imaging (Figs. 2a and b) and SEM imaging (Fig. S1 in Supporting information), both Co_9S_8 and CoPPD NSs exhibited regular spherical structure with uniform size distribution. In particular for CoPPD NSs, a distinct polymer shell was wrapped around the Co_9S_8 core, ascribed to the effective modification of PDA and PEG. The average diameters of Co_9S_8 and CoPPD NSs were measured to be 87.5 ± 2.7 and 92.1 ± 3.1 nm, respectively. Correspondingly, the thickness of nanoshell was calculated to be ~4.6 nm. Afterwards, the hydrodynamic sizes of Co_9S_8 and CoPPD NSs were quantified to be 111.1 and 141.8 nm, respectively, which are highly desirable for their enrichment in tumor size (Figs. 2c and d). Furthermore, zeta potentials of all intermediate and final products were quantified to elucidate the synthesis mechanism (Fig. 2e). Compared with −12 eV of pristine Co_8S_9 NSs, *in situ* growth of PDA contributed to a slight decrease of surface potential to −19.5 eV, owing to the integrative effect of the presence of catechol, quinone, amino, planar indole units and carboxylic acid groups in PDA chemical structures [49]. Zeta potential of CoPP NSs was measured to be −14.5 eV, suggesting an effective conjugation of PEG through the reaction of sulfhydryl group with quinone in PDA according to the Michael addition reaction [50]. Distinctly, the resultant CoPPD NSs displayed a surface potential of −9.2 eV, attributed to the successful drug encapsulation *via* hydrophobic interaction and π-π stacking between sp^2-bonded carbon skeleton and aromatic structure of DOX. FT-IR spectra were further measured to confirm the composition of CoPPD NSs (Fig. 2f). The strong absorption peaks of Co_9S_8 NSs at 1130 and 619.9 cm^{-1} can be assigned to the bending vibration of S—O group and stretching vibration of Co atoms, respectively. In addition, stretching vibrations of aromatic rings and C—O stretching of phenol contributed to the broad absorption bands of PDA in the range of 1800−1000 cm^{-1}. In SH-PEG, peaks at 1150 and 2890 cm^{-1} donated the stretching vibration of C—O—C and C—H groups, respectively. DOX showed a strong peak at ~1570 cm^{-1}, ascribed to the presence of N—H group. FTIR spectrum of CoPPD NSs exhibited all the characteristic peaks of these building blocks, implying a successful composite formation. The crystalline structure of Co_9S_8 NSs was further explored by using X-Ray diffraction (XRD), and the XPD pattern matched well with the phase of Co_9S_8 (JCPDS #65-6801) (Fig. S2 in Supporting information). In addition, strong Co and S signals in XPS full spectrum testified the elemental composition of Co_9S_8 NSs (Fig. S3a in Supporting information). The core level of the doublet peaks of Co $2p_{3/2}$ (778/793 eV) and Co $2p_{1/2}$ (782/797 eV) were assigned to Co^{3+} and Co^{2+} spin-orbit electrons of Co_9S_8, respectively (Fig. S3b in Supporting information). UV–vis-NIR absorbance

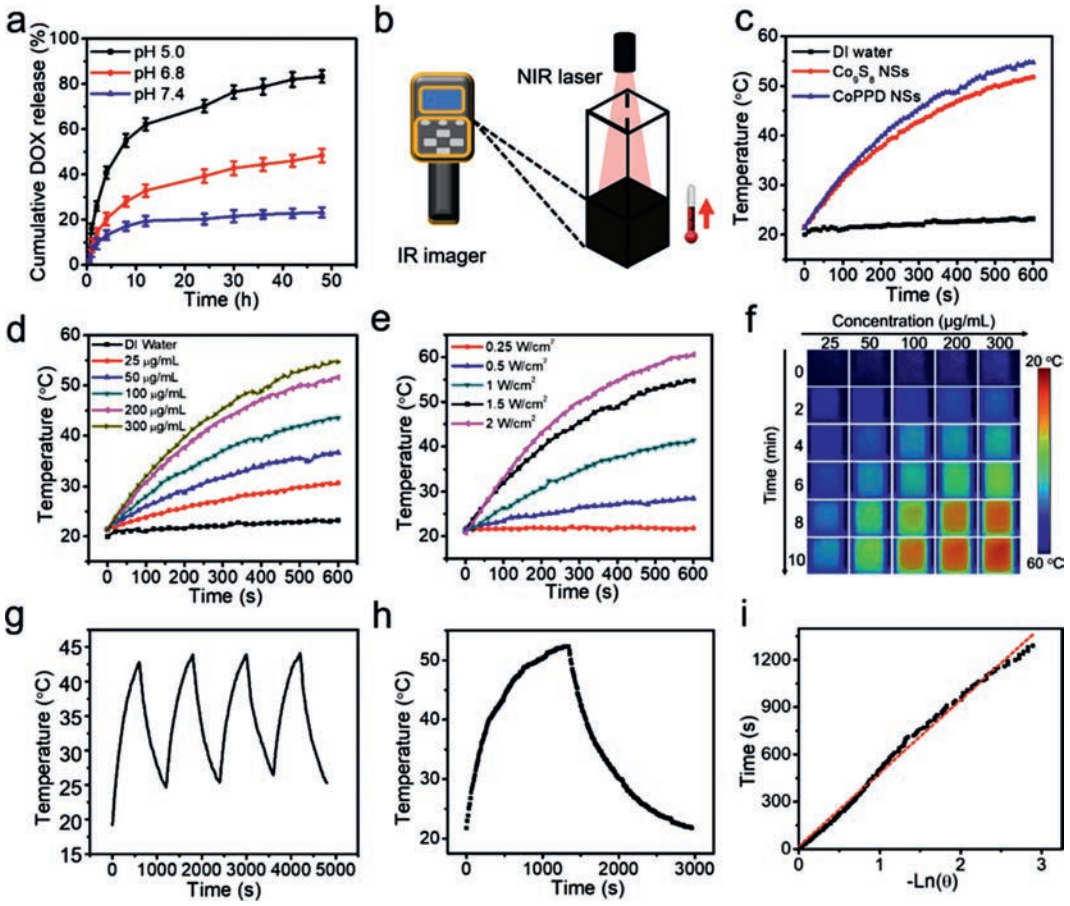

Fig. 3. (a) *In vitro* DOX release of CoPPD NSs under different pH conditions. (b) Schematic diagram to illustrate the setup for photothermal property evaluation. (c) Temperature elevation profile of the aqueous dispersion of Co_9S_8 (150 μg/mL) and CoPPD NSs (300 μg/mL) under NIR irradiation (808 nm, 1.5 W/cm^2) for 10 min. (d) Temperature elevation profile of CoPPD NSs with gradient concentrations within 10 min exposure to NIR light. (e) Temperature elevation profile of CoPPD NSs (300 μg/mL) subject to NIR laser irradiation at various output power densities. (f) Thermographic images of CoPPD NS dispersion in cuvettes upon 10 min NIR illumination. (g) Temperature change of CoPPD NSs (100 μg/mL) for four cycles (laser on: 10 min for each cycle). (h) Heating and cooling curve of CoPPD NSs (1 mL, 100 μg/mL). (i) Fitting curve of time *vs.* $-\ln(\theta)$ derived from the cooling stage in (h).

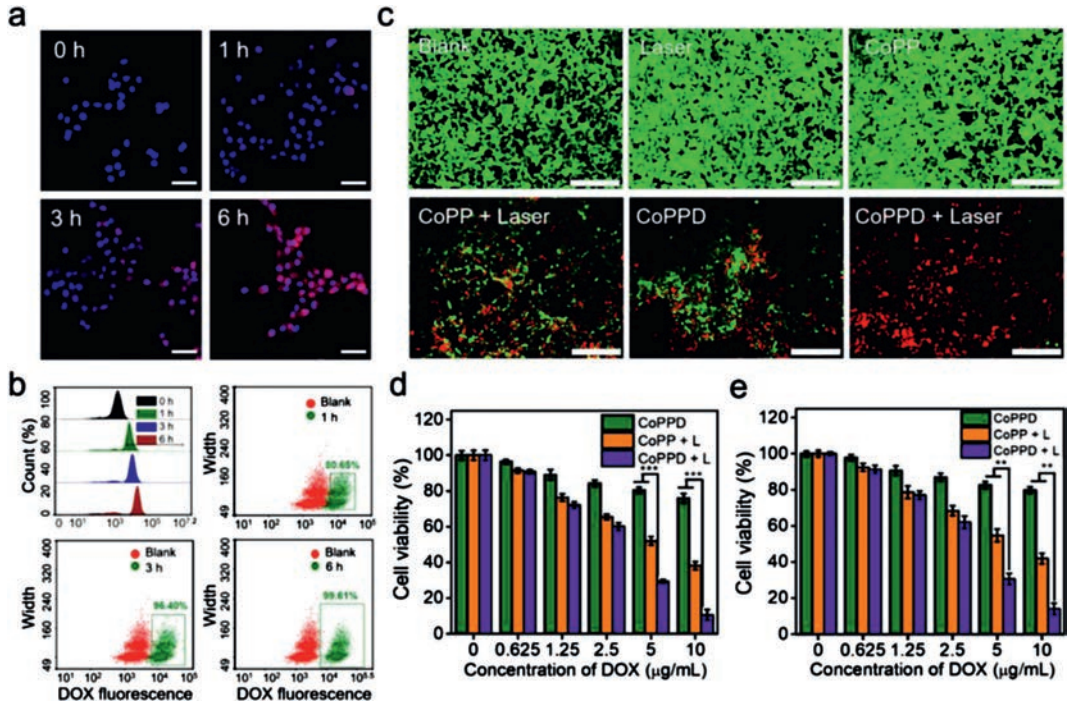

Fig. 4. Cellular study *in vitro*. (a) Fluorescence image of 4T1 cells after being treated by CoPPD NSs (equivalent DOX concentration: 10 μg/mL) for 1, 3 and 6 h (scale bar: 50 μm). (b) Flow cytometry diagram corresponding to (a). (c) LIVE/DEAD cell staining after 4T1 cell receiving various treatments (scale bar: 200 μm). Viability of (d) 4T1 and (e) HeLa cells after various treatments (**$P < 0.01$ and ***$P < 0.005$). NIR laser irradiation (808 nm, 1.5 W/cm^2) was performed for 5 min where applicable.

spectrum of CoPPD NSs exhibited a strong adsorption in NIR region, manifesting a promising potential to act as a PTA candidate (Fig. 2g). Notably, a unique characteristic peak was found in CoPPD NSs at 488 nm, strongly evidencing the effective loading of DOX. Moreover, the increment of absorption intensity was positively proportional to the concentration of CoPPD NSs, further verifying their good dispersity in aqueous condition (Fig. 2h). In another aspect, the fluorescence spectrum of CoPPD NSs exhibited negligible difference from that of free DOX under the excitation wavelength of 488 nm, which is highly recommended for tracking their intracellular distribution and biodistribution *in vivo* (Fig. 2i). Long-term storage stability of CoPPD NSs under physiological condition was evaluated by monitoring the hydrodynamic diameter in phosphate buffer saline (PBS), Dulbecco's modified eagle medium (DMEM) and fetal bovine serum (FBS, 10%) for seven days. No significant fluctuation in the hydrated size was observed during this period, implying an admirable stability of CoPPD NSs when circulating in bloodstream (Fig. S4 in Supporting information).

To currently achieve the maximum drug loading capacity (LC) and encapsulation efficiency (EE), different feeding ratios of DOX to CoPP NSs in weight (0.5, 1, 2, 3 and 4) were screened during the synthesis of CoPPD NSs. Based on spectrophotometry, the optimum combination was obtained at the weight ratio of 1:1 (DOX:CoPP), with LC and EE measured to be 44.6% and 45.2%, respectively (Fig. S5 in Supporting information). To explore stimulus-responsive drug release from CoPPD NSs, drug release profile of DOX was monitored under different pH conditions based on a standard dialysis method. As shown in Fig. 3a, the cumulative DOX release reached up to only ~23.2% at pH 7.4 within 48 h incubation. By contrast, more acidic conditions including pH 6.8 and pH 5.0 can effectively accelerate drug release, and the release amount of 48.4% and 93.3% was respectively attained during this period. Protonation of amino acid group in DOX may contribute to the pH-promoted drug release, *via* weakening drug binding affinity and enhancing drug solubility. Therefore, we anticipated that the indiscriminate attack of CoPPD NSs toward normal cells can be effectively circumvented to avoid severer systemic toxicity.

Taking advantage of strong NIR absorption, photothermal property of CoPPD NSs was explored by illuminating sample-laden cuvette with an NIR laser (808 nm, 1.5 W/cm^2) for 10 min (Fig. 3b). The terminal temperature of CoPPD NSs (300 μg/mL) arrived to 54.7 °C, dramatically higher than 23.2 °C of DI water, manifesting a promising perspective for hyperthermia-induced tumor damage (Fig. 3c). It was also found that elevation magnitude of CoPPD NSs relied on not only the agent concentration (25−300 μg/mL) but also the output power density of NIR laser (0.25–2 W/cm^2) (Figs. 3d and e). The thermographic images further testified the laser-induced temperature rising mediated by CoPPD NSs (Fig. 3f). To assess the photothermal stability of CoPPD NSs, four consecutive On/Off laser irradiation cycles was implemented (laser on for 10 min for each cycle). And, no observable decay of the elevated magnitude of sample temperature was found before and after cyclic laser exposure (Fig. 3g). The photothermal conversion efficiency (η) of CoPPD NSs was determined to be 49.97% as derived from Figs. 3h and i. These results implied an admirable photothermal stability and conversion capacity of CoPPD NSs for clinical translations.

To understand the uptake of CoPPD NSs by tumor cells, fluorescence signal of DOX in CoPPD-treated 4T1 cells was tracked after incubation for 0, 1, 3 and 6 h (Fig. 4a). The internalized of CoPPD NSs was primarily distributed in the cytoplasm, and cellular uptake was highly dependent on the incubation time, as evidenced by the progressively upgraded intracellular fluorescence level from 0 to 6 h based on flow cytometry analysis (Fig. 4b). The percentage of cells that took in a significant quantity of CoPPD NSs was calculated to be 99.61% after 6 h incubation, suggesting a highly efficient intracellular localization. Afterwards, biocompatibility of CoPP NSs as the drug carrier was investigated on normal cells of both human umbilical vein endothelial cells (HUVECs) and murine L929 fibrosarcoma cells (L929 s). After incubation with CoPP NSs at

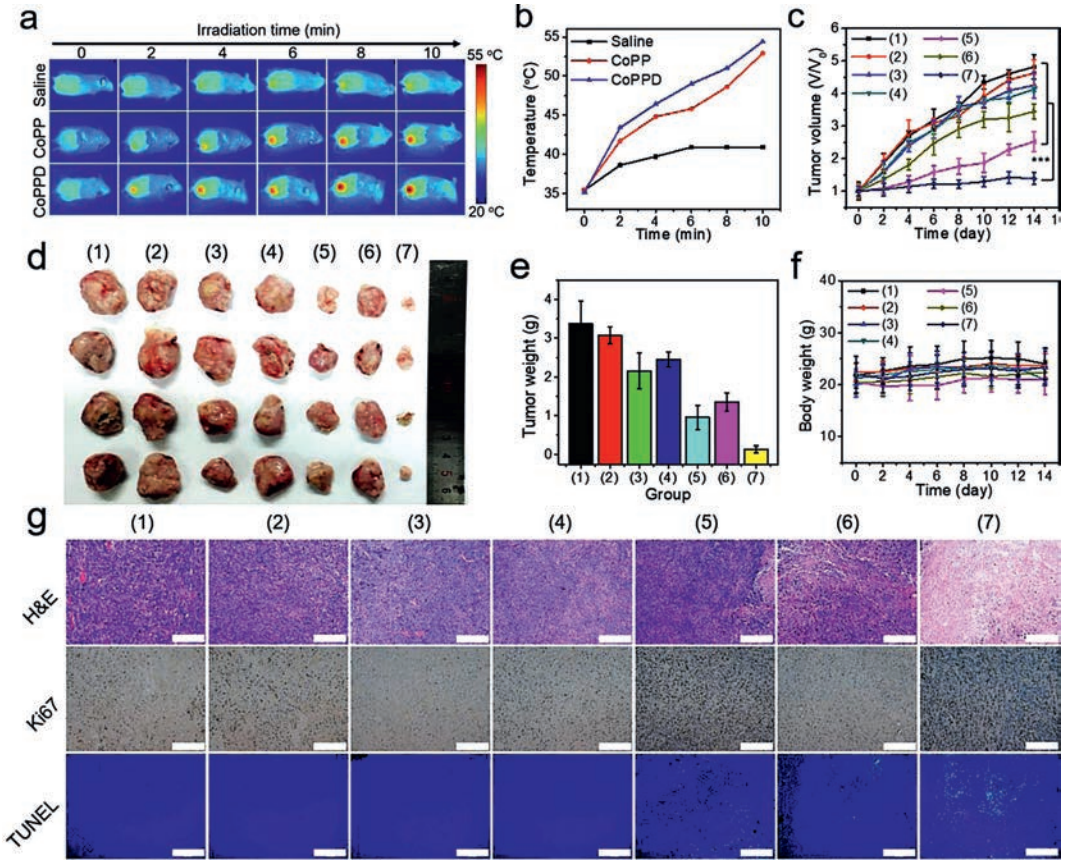

Fig. 5. Antitumor effect *in vivo*. (a) Thermographic image of tumor-bearing mice during laser irradiation (808 nm, 1.5 W/cm^2) toward tumor site for 10 min upon the injection of various agents. (b) Average temperature at tumor region during NIR irradiation corresponding to (a). (c) Change in tumor volume during the course of 14 days after various treatments (***$P < 0.005$ compared to any other group). (d) Digital photographs and (e) average weight of the dissected solid tumor on day 14. (f) Variation of mouse body weight in two weeks after different administrations. (g) Histopathological analysis of tumor section *via* H&E, TUNEL and Ki67 staining (scale bar: 200 μm). Group 1-7: saline, NIR laser, free DOX, CoPP, CoPP + laser, CoPPD, CoPPD + laser.

diversified concentrations for 24 h, cell viability still exceeded 90% at a dramatically high concentration of 200 μg/mL, indicating an admirable biocompatibility for systemic applications (Fig. S6 in Supporting information). Furthermore, tumor cell killing effect caused by photo-activated hyperthermia was investigated on 4T1 cells through LIVE/DEAD cell fluorescence staining (Fig. 4c). Similar with the blank control group (without any treatment), only laser or CoPP drug carrier showed negligible adverse effect on cell viability. By contrast, mild cell killing effect was found in the groups of "CoPP + Laser" and "CoPPD", as evidenced by the incorporated red dots among pervasive green ones, attributed to the representative photothermal and chemotherapeutic effect, respectively. Notably, "CoPPD + laser" led to the most remarkable tumor cell destruction, as revealed by bright red fluorescence emission from the entire laser irradiation zone, thanks to the intense chemotherapeutic-enhanced PTT. Afterwards, MTT assay was carried out to quantitatively investigate the viability of 4T1 cells after different treatments (Fig. 4d). As expected, the maximum reduction of cell viability was similarly found in the cells receiving the treatment of CoPPD plus laser irradiation. Such cytotoxicity exhibited a typical dose-dependent trend, and the lowest cell viability was achieved to be 10.6% at the equivalent DOX concentration of 10 μg/mL, which agreed well with the findings in fluorescence staining assay and further validated the strong PTT/chemotherapeutic combinatorial effect. In addition, the deleterious cytotoxicity effect caused by "CoPPD + laser" was also demonstrated on HeLa cells (Fig. 4e). To explore the hyperthermia-induced cell apoptosis, mitochondrial membrane potential (MMP), as a critical indicator of mitochondria status, was measured by using JC-1 assay (Fig. S7 in Supporting information). The most remarkable increase in green fluorescence intensity and reduction in orange fluorescence intensity were concurrently found in the group of "CoPP + laser", which suggested an outstanding conversion of JC-1 existing form from aggregates to monomers, reflecting the progressive cell apoptosis caused by local thermal generation.

To evaluate the tumor suppression effect *in vivo*, BALB/c mice bearing 4T1 tumors were randomly allocated into seven groups, including group 1 (saline), group 2 (NIR laser), group 3 (free DOX), group 4 (CoPP), group 5 (CoPP + laser), group 6 (CoPPD) and group 7 (CoPPD + laser). At 24 h post-injection, NIR laser irradiation toward tumor site was conducted for 10 min in group 2, 5 and 7. Infrared thermography was carried out to real-time monitor the local temperature elevation. A shown in Figs. 5a and b, rapid local heating was observed in groups 5 and 7 during laser irradiation for 10 min, and final temperature were measured to be 52.9 °C and 54.4 °C, respectively. The results implied a decent hyperthermia generation effect *via* photo-activation. Thereafter, tumor volume change was dynamically monitored during 14 days post-administration (Figs. 5c and d). Compared with saline control, treatments of NIR laser, free DOX and CoPP displayed insignificant tumor inhibitory effect, as evidenced by the similar trend in tumor volume increase among these four groups. In comparison, a certain degree of tumor growth suppression was found in the groups of "CoPP + laser" and "CoPPD" with inhibition indexes of 47.8% and

28.4%, resulting from the respective effect of PTT and chemotherapy. Remarkably, "CoPPD + laser" led to the most significant tumor eradication, with an inhibition index as much as 71.1% after two weeks post-treatment, which can be attributed to the passive tumor targeting of CoPPD *via* enhanced permeation retention (EPR) effect and subsequent strong chemotherapeutic-enhanced PTT. In addition, tumor weight also followed a similar trend with the ultimate tumor volume (Fig. 5e). In another aspect, body weight of animal models was not significantly fluctuated in all groups, indicating minimal adverse effect caused by all treatment formulations (Fig. 5f). Finally, H&E and Ki67 staining, as well as TUNEL immunofluorescence assay were carried out to investigate the tissue damage at the histological level (Fig. 5g). In accordance with the results in tumor suppression, the most severe nuclear condensation and membrane fragmentation was discovered in the group of "CoPPD + laser", in a sharp contrast to the regular morphology in saline group. Besides, the highest level of both cell apoptosis and inhibition of cell proliferation were found in the same treatment group, as verified by the most pervasive green fluorescence emission from TUNEL assay and the minimum quantity of Ki67 positive cells (browned-colored nuclei), respectively. To explore the biosafety of the administration of "CoPPD + laser", H&E staining was performed on the slices of major organs excised on day 14 (Fig. S8 in Supporting information). There was no apparent morphological abnormality at the tissue level for all groups, implying an extremely low toxicity caused by all these treatment recipes. On the other hand, hemolytic assay was performed to understand the hemocompatibility of CoPPD NSs, through incubating red blood cells (RBCs) with different agents (Fig. S9 in Supporting information). The hemolytic rate was increased with CoPPD concentration in the range of 10–200 μg/mL, and the maximum value was measured to be only 4.45% after 8 h incubation, which was ideal for long-term blood circulation.

In summary, we have successfully engineered PDA-activated CoS NSs based on a modified solvothermal-based strategy, which can effectively resolve the challenges in the functionalization of CoS surface for medical applications. Moreover, PEG and DOX were successfully modified on the surface of such PDA-activated CoS NSs, which endowed the nanocarrier with the potency of serving as not only light achievable PTA but also acidity-inducible drug release. The resultant CoPPD NSs can trigger an effective chemotherapeutic-enhanced PTT, as demonstrated in both cellular studies and animal experiments. Moreover, the proposed treatment regimen exhibited reliable biosafety without causing observable side effects. Taken together, this study may definitely extend the development of more CoS-based functional nanocomposites, which are potentially treasurable for clinical translations.

Declaration of competing interest

The authors declare that they have no known competing financial interests or personal relationships that could have appeared to influence the work reported in this paper.

Acknowledgment

This project was supported by National Natural Science Foundation of China (Nos. 51703186, 31671037).

Appendix A. Supplementary data

Supplementary material related to this article can be found, in the online version, at doi:https://doi.org/10.1016/j.cclet.2020.08.009.

References

[1] R.L. Siegel, K.D. Miller, A. Jemal, CA-Cancer J. Clin. 70 (2020) 7–30.
[2] J. Ferlay, M. Colombet, I. Soerjomataram, et al., Int. J. Cancer 144 (2019) 1941–1953.
[3] D.G. You, V.G. Deepagan, W. Um, et al., Sci. Rep. 6 (2016) 23200.
[4] T. Yu, Y. Hu, G. Feng, K. Hu, Adv. Ther. 3 (2020) 2070005.
[5] P. Wang, S. Sun, H. Ma, et al., Mater. Sci. Eng. C 108 (2020) 110198.
[6] J. Wang, X. Wu, P. Shen, et al., Int. J. Nanomed. 15 (2020) 1903–1914.
[7] Y. Xiao, J. Peng, Q. Liu, et al., Theranostics 10 (2020) 1500–1513.
[8] S. Yang, L. Zhou, Y. Su, et al., Chin. Chem. Lett. 30 (2019) 187–191.
[9] Q.W. Tian, F.R. Jiang, R.J. Zou, et al., ACS Nano 5 (2011) 9761–9771.
[10] L. Zou, H. Wang, B. He, et al., Theranostics 6 (2016) 762–772.
[11] P. Rai, S. Mallidi, X. Zheng, et al., Adv. Drug Deliv. Rev. 62 (2010) 1094–1124.
[12] M.M. Gao, L.L. Zhu, C.K. Peh, G.W. Ho, Energy Environ. Sci. 12 (2019) 841–864.
[13] S. Liu, J. Pan, J. Liu, et al., Small 14 (2018) 1703968.
[14] Q. Wang, Y.N. Dai, J.Z. Xu, et al., Adv. Funct. Mater. 29 (2019) 1901480.
[15] W. Chen, J. Ouyang, H. Liu, et al., Adv. Mater. 29 (2017) 1603864.
[16] J. Yang, S. Zhai, H. Qin, et al., Biomaterials 176 (2018) 1–12.
[17] X. Li, Y. Zhang, Z. Ma, et al., Chin. Chem. Lett. 30 (2019) 489–493.
[18] Q. Guo, D. Wang, G. Yang, J. Biomed. Nanotechnol. 15 (2019) 2090–2099.
[19] D. Hu, L. Chen, Y. Qu, et al., Theranostics 8 (2018) 1558–1574.
[20] X. Chen, X. Liu, K. Huang, Chin. Chem. Lett. 30 (2019) 797–800.
[21] X. Cheng, R. Sun, L. Yin, et al., Adv. Mater. 29 (2017) 1604894.
[22] M. Mirrahimi, Z. Abed, J. Beik, et al., Pharmacol. Res. 143 (2019) 178–185.
[23] Y.W. Chen, Y.L. Su, S.H. Hu, S.Y. Chen, Adv. Drug Deliv. Rev. 105 (2016) 190–204.
[24] X. Jiang, S. Zhang, F. Ren, et al., ACS Nano 11 (2017) 5633–5645.
[25] X. Wang, Z. Miao, Y. Ma, et al., Nanoscale 9 (2017) 14512–14519.
[26] K. Liu, K. Liu, J.C. Liu, et al., Nanoscale 12 (2020) 2902–2913.
[27] H.L. Yang, J.L. Zhao, C.Y. Wu, et al., Chem. Eng. J. 351 (2018) 548–558.
[28] X. Wang, Y. Ma, X. Sheng, et al., Nano Lett. 18 (2018) 2217–2225.
[29] B. Guo, J. Zhao, C. Wu, et al., Colloids Surf. B 177 (2019) 346–355.
[30] B. Xia, B. Wang, J. Shi, et al., Acta Biomater. 51 (2017) 197–208.
[31] H.S. Jung, P. Verwilst, A. Sharma, et al., Chem. Soc. Rev. 47 (2018) 2280–2297.
[32] L. Gan, M. Qian, K. Shi, et al., Neural Regener. Res. 9 (2014) 1979–1984.
[33] R.V. Jagadeesh, T. Stemmler, A.E. Surkus, et al., Nat. Protoc. 10 (2015) 916–926.
[34] L. Zhong, D. Hu, Y. Qu, et al., J. Biomed. Nanotechnol. 15 (2019) 857–877.
[35] C.H. Wu, C. Liu, D. Su, et al., Nat. Catal. 2 (2019) 78–85.
[36] Y.Q. Zhao, B. Jin, Y. Zheng, et al., Adv. Energy Mater. 8 (2018) 1801926.
[37] Y. Hao, Y. Liu, R. Yang, et al., Chin. Chem. Lett. 29 (2018) 778–782.
[38] J. Yang, C. Yu, X.M. Fan, et al., Energy Environ. Sci. 9 (2016) 1299–1307.
[39] A.M. Elshahawy, C. Guan, X. Li, et al., Nano Energy 39 (2017) 162–171.
[40] N.S. Nguyen, G. Das, H.H. Yoon, Biosens. Bioelectron. 77 (2016) 372–377.
[41] S. Chaiyo, E. Mehmeti, W. Siangproh, et al., Biosens. Bioelectron. 102 (2018) 113–120.
[42] S.B. Lin, Y.Y. Wang, Z.Z. Chen, et al., ACS Sustainable Chem. Eng. 6 (2018) 12061–12069.
[43] G. Guan, X. Wang, X. Huang, et al., Nanoscale 10 (2018) 14190–14200.
[44] Z.L. Li, Z. Li, L. Chen, et al., Nano Res. 11 (2018) 2436–2449.
[45] X.W. Wang, X.Y. Zhong, Z.B. Zha, et al., Appl. Mater. Today 18 (2020) 100464.
[46] D. Bi, L. Zhao, R. Yu, et al., Drug Deliv. 25 (2018) 564–575.
[47] S. Zhao, M. Golestani, A. Penesyan, et al., Chin. Chem. Lett. 31 (2020) 851–854.
[48] R. Wu, H.Z. Wang, L. Hai, et al., Chin. Chem. Lett. 31 (2020) 189–192.
[49] L. Zhang, H. Su, J. Cai, et al., ACS Nano 10 (2016) 10404–10417.
[50] P. Xue, L. Sun, Q. Li, et al., Colloids Surf. B 160 (2017) 11–21.